Article

Kinetics of Monodisperse Iron Oxide Nanocrystal Formation by "Heating-Up" Process

Soon Gu Kwon, Yuanzhe Piao, Jongnam Park, Subramanian Angappane, Younghun Jo, Nong-Moon Hwang, Je-Geun Park, and Taeghwan Hyeon

J. Am. Chem. Soc., **2007**, 129 (41), 12571-12584• DOI: 10.1021/ja074633q • Publication Date (Web): 22 September 2007

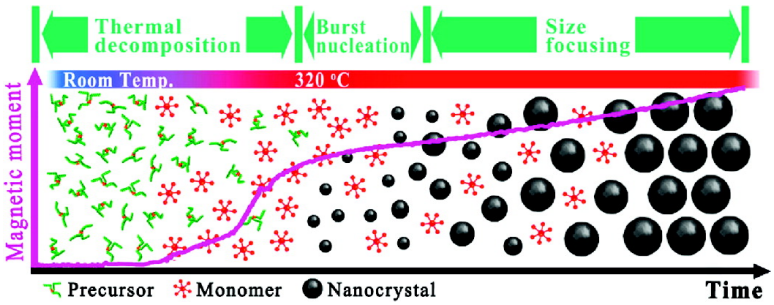

More About This Article

Additional resources and features associated with this article are available within the HTML version:

- Supporting Information
- Links to the 10 articles that cite this article, as of the time of this article download
- Access to high resolution figures
- Links to articles and content related to this article
- Copyright permission to reproduce figures and/or text from this article

View the Full Text HTML

J|A|C|S
ARTICLES
Published on Web 09/22/2007

Kinetics of Monodisperse Iron Oxide Nanocrystal Formation by "Heating-Up" Process

Soon Gu Kwon,[†] Yuanzhe Piao,[†] Jongnam Park,[†] Subramanian Angappane,[‡] Younghun Jo,[§] Nong-Moon Hwang,[||] Je-Geun Park,[‡] and Taeghwan Hyeon*,[†]

Contribution from the National Creative Research Initiative Center for Oxide Nanocrystalline Materials, and School of Chemical and Biological Engineering, Seoul National University, Seoul 151-744, Korea, Department of Physics and Institute of Basic Science, Sungkyunkwan University, Suwon 440-746, Korea, Quantum Material Research Team, Korea Basic Science Institute, Daejeon 305-333, Korea, and School of Materials Science & Engineering and National Research Laboratory of Charged Nanoparticles, Seoul National University, Seoul 151-744, Korea

Received June 25, 2007; E-mail: thyeon@snu.ac.kr

Abstract: We studied the kinetics of the formation of iron oxide nanocrystals obtained from the solution-phase thermal decomposition of iron−oleate complex via the "heating-up" process. To obtain detailed information on the thermal decomposition process and the formation of iron oxide nanocrystals in the solution, we performed a thermogravimetric-mass spectrometric analysis (TG-MS) and in-situ magnetic measurements using SQUID. The TG-MS results showed that iron−oleate complex was decomposed at around 320 °C. The in-situ SQUID data revealed that the thermal decomposition of iron−oleate complex generates intermediate species, which seem to act as monomers for the iron oxide nanocrystals. Extensive studies on the nucleation and growth process using size exclusion chromatography, the crystallization yield data, and TEM showed that the sudden increase in the number concentration of the nanocrystals (burst of nucleation) is followed by the rapid narrowing of the size distribution (size focusing). We constructed a theoretical model to describe the "heating-up" process and performed a numerical simulation. The simulation results matched well with the experimental data, and furthermore they are well fitted to the well-known LaMer model that is characterized by the burst of nucleation and the separation of nucleation and growth under continuous monomer supply condition. Through this theoretical work, we showed that the "heating-up" and "hot injection" processes could be understood within the same theoretical framework in which they share the characteristics of nucleation and growth stages.

Introduction

For the last 20 years, the synthesis of nanocrystals has been intensively pursued not only for their fundamental scientific interest, but also for their many technological applications.[1] The synthesis of uniform-sized (or monodisperse with a relative standard deviation of $\leq 5\%$) nanocrystals is of key importance because the properties of these nanocrystals depend strongly on their dimensions.[2] From the fundamental scientific viewpoint, the synthesis of uniform-sized nanocrystals with controllable sizes is very important to characterize the size-dependent physical properties of nanocrystals.[2e−i] On the other hand, the production of large quantities of uniform-sized nanocrystals will become critical for the realization of high-quality nanoscale devices and many high-end nanotechnological applications. For example, the color sharpness of semiconductor nanocrystal-based optical devices and biomedical imaging probes is strongly dependent on the uniformity of the nanocrystals,[3] and monodisperse magnetic nanocrystals can be used as multi-terabit (Tbit/in^2) magnetic storage media.[4] Over the past decade, remarkable advances have been made in the synthesis of uniform-sized colloidal nanocrystals.[5] However, our understanding of the

[†] School of Chemical and Biological Engineering, Seoul National University.
[‡] Sungkyunkwan University.
[§] Korea Basic Science Institute.
[||] School of Materials Science & Engineering, Seoul National University.

(1) (a) Fendler, J. H., Ed. *Nanoparticles and Nanostructured Films*; Wiley-VCH: Weinheim, 1998. (b) Klabunde, K. J., Ed. *Nanoscale Materials in Chemistry*; Wiley-Interscience: New York, 2001. (c) Schmid, G., Ed. *Nanoparticles*; Wiley-VCH: Weinheim, 2004. (d) Alivisatos, A. P. *Science* **1996**, *271*, 933. (e) Rogach, A. L.; Talapin, D. V.; Shevchenko, E. V.; Kornowski, A.; Haase, M.; Weller, H. *Adv. Funct. Mater.* **2002**, *12*, 653. (f) Hyeon, T. *Chem. Commun.* **2003**, 927.

(2) (a) Bawendi, M. G.; Steigerwald, M. L.; Brus, L. E. *Annu. Rev. Phys. Chem.* **1990**, *41*, 477. (b) Batlle, X.; Labarta, A. *J. Phys. D: Appl. Phys.* **2002**, *35*, R15. (c) El-Sayed, M. A. *Acc. Chem. Res.* **2001**, *34*, 257. (d) Xu, Z.; Xiao, F.-S.; Purnell, S. K.; Alexeev, O.; Kawi, S.; Deutsch, S. E.; Gates, B. C. *Nature* **1994**, *372*, 346. (e) Spanhel, L.; Haase, M.; Weller, H.; Henglein, A. *J. Am. Chem. Soc.* **1987**, *109*, 5649. (f) Steigerwald, M. L.; Brus, L. E. *Annu. Rev. Mater. Sci.* **1989**, *19*, 471. (g) Steigerwald, M. L.; Brus, L. E. *Acc. Chem. Res.* **1990**, *23*, 183. (h) Goldstein, A. N.; Echer, C. M.; Alivisatos, A. P. *Science* **1992**, *256*, 1425. (i) Alivisatos, A. P. *J. Phys. Chem.* **1996**, *100*, 13226.

(3) (a) Bruchez, M., Jr.; Moronne, M.; Gin, P.; Weiss, S.; Alivisatos, A. P. *Science* **1998**, *281*, 2013. (b) Chan, W. C. W.; Nie, S. *Science* **1998**, *281*, 2016. (c) Medintz, I. L.; Uyeda, H. T.; Goldman, E. R.; Mattoussi, H. *Nat. Mater.* **2005**, *4*, 435. (d) Michalet, X.; Pinaud, F. F.; Bentolila, L. A.; Tsay, J. M.; Doose, S.; Li, J. J.; Sundaresan, G.; Wu, A. M.; Gambhir, S. S.; Weiss, S. *Science* **2005**, *307*, 538. (e) Klostranec, J. M.; Chan, W. C. W. *Adv. Mater.* **2006**, *18*, 1953.

mechanism of formation of these uniform-sized nanocrystals is still very limited.

In 1993, Bawendi and his colleagues reported the synthesis of uniform-sized cadmium chalcogenide nanocrystals using a technique that is now well-known as the "hot injection" method.[6] This "hot injection" method has been widely used to synthesize nanocrystals of II−VI,[7] III−V,[8] and lead chalcogenide semiconductors,[9] and transition metals.[4b,9a,10] Although the detailed procedures used for the synthesis of nanocrystals vary depending on the materials involved, a similar strategy is generally employed to produce uniform nanocrystals, in which high supersaturation is induced by the rapid injection of the highly reactive reactants into a hot surfactant solution. The underlying mechanism of the "hot injection" process has been well studied both theoretically and experimentally. The previous extensive works on the synthesis of micrometer-scale particles revealed that the burst of nucleation and subsequent size focusing growth process are critical for the formation of monodisperse particles.[11] A similar principle is applied to the synthesis of monodisperse nanoparticles via the "hot injection" methods. High supersaturation induced by "hot injection" leads to the fast homogeneous nucleation reaction that is followed by the diffusion-controlled growth process, in which "focusing" of the particle size distribution occurs.[6,12] That is, the process of the size distribution narrowing for the "hot injection" method is a kinetically driven one that is initiated by high initial supersaturation.[5a] Most studies on the size distribution control mechanism in the "hot injection" process have been conducted on semiconductor nanocrystals (quantum dots, QDs), because these QDs exhibit characteristic size-dependent optical properties.[13] These mechanistic studies using optical absorption and photoluminescence spectra revealed that the burst of nucleation followed by the size "focusing" actually occurs in the "hot injection" process for the synthesis of II−VI and III−V QDs.[7a,12a,14]

There are other synthetic methods that produce uniform nanocrystals with a size distribution comparable to that obtained using the "hot injection" method.[5b] Among them, the so-called "heating-up" method, in which the reaction solution prepared at low temperature is heated to high temperature to produce nanoparticles, has been extensively used to synthesize monodisperse nanocrystals of transition metals[4c,15] and metal oxides.[15a,16] For example, our group reported on the synthesis of highly monodisperse iron oxide nanocrystals by the solution-phase thermal decomposition of iron−oleate complex.[17] Although the "heating-up" process has been widely used for the synthesis of uniform nanocrystals of various materials, very few mechanistic studies have been conducted, because there is no readily available characterization method that can be used to follow the nucleation and growth process. The "heating-up" method is quite different from the "hot injection" method in that there is no operation that induces high supersaturation instantaneously. The mechanism underlying the control of the size distribution

(4) (a) Speliotis, D. E. *J. Magn. Magn. Mater*. **1999**, *193*, 29. (b) Sun, S.; Murray, C. B. *J. Appl. Phys.* **1999**, *85*, 4325. (c) Sun, S.; Murray, C. B.; Weller, D.; Folks, L.; Moser, A. *Science* **2000**, *287*, 1989. (d) Moser, A.; Takano, K.; Margulies, D. T.; Albrecht, M.; Sonobe, Y.; Ikeda, Y.; Sun, S.; Fullerton, E. E. *J. Phys. D: Appl. Phys.* **2002**, *35*, R157.

(5) Comprehensive reviews on the synthesis of nanocrystals: (a) Yin, Y.; Alivisatos, A. P. *Nature* **2005**, *437*, 664. (b) Park, J.; Joo, J.; Kwon, S. G.; Jang, Y.; Hyeon, T. *Angew. Chem., Int. Ed.* **2007**, *46*, 4630. On the synthesis of semiconductor nanocrystals: (c) El-Sayed, M. A. *Acc. Chem. Res.* **2004**, *37*, 326. (d) Donegá, C. d. M.; Liljeroth, P.; Vanmaekelbergh, D. *Small* **2005**, *1*, 1152. On the synthesis of magnetic nanocrystals: (e) Jeong, U.; Teng, X.; Wang, Y.; Yang, H.; Xia, Y. *Adv. Mater.* **2007**, *19*, 33. (f) Lu, A.-H.; Salabas, E. L.; Schüth, F. *Angew. Chem., Int. Ed.* **2007**, *46*, 1222. On the synthesis of noble metal nanoparticles: (g) Wiley, B.; Sun, Y.; Mayers, B.; Xia, Y. *Chem.-Eur. J.* **2005**, *11*, 454. (h) Eustis, S.; El-Sayed, M. A. *Chem. Soc. Rev.* **2006**, *35*, 209. On the synthesis of anisotropic nanocrystals: (i) Xia, Y.; Yang, P.; Sun, Y.; Wu, Y.; Mayers, B.; Gates, B.; Yin, Y.; Kim, F.; Yan, H. *Adv. Mater.* **2003**, *15*, 353. (j) Burda, C.; Chen, X.; Narayanan, R.; El-Sayed, M. A. *Chem. Rev.* **2005**, *105*, 1025. (k) Jun, Y.-w.; Choi, J.-s.; Cheon, J. *Angew. Chem., Int. Ed.* **2006**, *45*, 3414. (l) Kumar, S.; Nann, T. *Small* **2006**, *2*, 316.

(6) Murray, C. B.; Norris, D. J.; Bawendi, M. G. *J. Am. Chem. Soc.* **1993**, *115*, 8706.

(7) (a) Talapin, D. V.; Rogach, A. L.; Kornowski, A.; Haase, M.; Weller, H. *Nano Lett.* **2001**, *1*, 207. (b) Katari, J. E. B.; Colvin, V. L.; Alivisatos, A. P. *J. Phys. Chem.* **1994**, *98*, 4109. (c) Qu, L.; Peng, Z. A.; Peng, X. *Nano Lett.* **2001**, *1*, 333. (d) Peng, Z. A.; Peng, X. *J. Am. Chem. Soc.* **2001**, *123*, 183. (e) Yu, W. W.; Peng, X. *Angew. Chem., Int. Ed.* **2002**, *41*, 2368. (f) Hines, M. A.; Guyot-Sionnest, P. *J. Phys. Chem. B* **1998**, *102*, 3655. (g) Li, L. S.; Pradhan, N.; Wang, Y.; Peng, X. *Nano Lett.* **2004**, *4*, 2261.

(8) (a) Guzelian, A. A.; Banin, U.; Kadavanich, A. V.; Peng, X.; Alivisatos, A. P. *Appl. Phys. Lett.* **1996**, *69*, 1432. (b) Cao, Y. W.; Banin, U. *J. Am. Chem. Soc.* **2000**, *122*, 9692. (c) Battaglia, D.; Peng, X. *Nano Lett.* **2002**, *2*, 1027.

(9) (a) Murray, C. B.; Sun, S.; Gaschler, W.; Doyle, H.; Betley, T. A.; Kagan, C. R. *IBM J. Res. Dev.* **2001**, *45*, 47. (b) Yu, W. W.; Falkner, J. C.; Shih, B. S.; Colvin, V. L. *Chem. Mater.* **2004**, *16*, 3318. (c) Lu, W.; Fang, J.; Stokes, K. L.; Lin, J. *J. Am. Chem. Soc.* **2004**, *126*, 11798.

(10) (a) Puntes, V. F.; Krishnan, K. M.; Alivisatos, A. P. *Appl. Phys. Lett.* **2001**, *78*, 2187. (b) Murray, C. B.; Sun, S.; Doyle, H.; Betley, T. *Mater. Res. Bull.* **2001**, *26*, 985. (c) Shevchenko, E. V.; Talapin, D. V.; Rogach, A. L.; Kornowski, A.; Haase, M.; Weller, H. *J. Am. Chem. Soc.* **2002**, *124*, 11480. (d) Park, J.; Kang, E.; Son, S. U.; Park, H. M.; Lee, M. K.; Kim, J.; Kim, K. W.; Noh, H.-J.; Park, J.-H.; Bae, C. J.; Park, J.-G.; Hyeon, T. *Adv. Mater.* **2005**, *17*, 429.

(11) (a) LaMer, V. K.; Dinegar, R. H. *J. Am. Chem. Soc.* **1950**, *72*, 4847. (b) Reiss, H. *J. Chem. Phys.* **1951**, *19*, 482. (c) Sugimoto, T. *Adv. Colloid Interface Sci.* **1987**, *28*, 65. (d) Sugimoto, T. *Monodispersed Particles*; Elsevier: New York, 2001.

(12) (a) Peng, X.; Wickham, J.; Alivisatos, A. P. *J. Am. Chem. Soc.* **1998**, *120*, 5343. (b) Peng, X.; Manna, L.; Yang, W.; Wickham, J.; Scher, E.; Kadavanich, A.; Alivisatos, A. P. *Nature* **2000**, *404*, 59. (c) Peng, Z. A.; Peng, X. *J. Am. Chem. Soc.* **2002**, *124*, 3343. (d) Talapin, D. V.; Rogach, A. L.; Haase, M.; Weller, H. *J. Phys. Chem. B* **2001**, *105*, 12278. (e) Talapin, D. V.; Rogach, A. L.; Shevchenko, E. V.; Kornowski, A.; Haase, M.; Weller, H. *J. Am. Chem. Soc.* **2002**, *124*, 5782.

(13) (a) Mikulec, F. V.; Kuno, M.; Bennati, M.; Hall, D. A.; Griffin, R. G.; Bawendi, M. G. *J. Am. Chem. Soc.* **2000**, *122*, 2532. (b) Schmelz, O.; Mews, A.; Basché, T.; Herrmann, A.; Müllen, K. *Langmuir* **2001**, *17*, 2861. (c) Yu, W. W.; Qu, L.; Guo, W.; Peng, X. *Chem. Mater.* **2003**, *15*, 2854.

(14) (a) Bullen, C. R.; Mulvaney, P. *Nano Lett.* **2004**, *4*, 2303. (b) Embden, J. v.; Mulvaney, P. *Langmuir* **2005**, *21*, 10226.

(15) (a) Hyeon, T.; Lee, S. S.; Park, J.; Chung, Y.; Na, H. B. *J. Am. Chem. Soc.* **2001**, *123*, 12798. (b) Chen, M.; Nikles, D. E. *Nano Lett.* **2002**, *2*, 211. (c) Chen, M.; Nikles, D. E. *J. Appl. Phys.* **2002**, *91*, 8477. (d) Kim, S.-W.; Park, J.; Jang, Y.; Chung, Y.; Hwang, S.; Hyeon, T.; Kim, Y. W. *Nano Lett.* **2003**, *3*, 1289. (e) Lin, X. Z.; Teng, X.; Yang, H. *Langmuir* **2003**, *19*, 10081. (f) Liu, C.; Wu, X.; Klemmer, T.; Shukla, N.; Yang, X.; Weller, D.; Roy, A. G.; Tanase, M.; Laughlin, D. *J. Phys. Chem. B* **2004**, *108*, 6121. (g) Chen, M.; Liu, J. P.; Sun, S. *J. Am. Chem. Soc.* **2004**, *126*, 8394. (h) Son, S. U.; Park, I. K.; Park, J.; Hyeon, T. *Chem. Commun.* **2004**, 778.

(16) Synthesis of metal ferrite nanocrystals: (a) Sun, S.; Zeng, H. *J. Am. Chem. Soc.* **2002**, *124*, 8204. (b) Jana, N. R.; Chen, Y.; Peng, X. *Chem. Mater.* **2004**, *16*, 3931. (c) Yu, W. W.; Falkner, J. C.; Yavuz, C. T.; Colvin, V. L. *Chem. Commun.* **2004**, 2306. (d) Redl, F. X.; Black, C. T.; Papaefthymiou, G. C.; Sandstrom, R. L.; Yin, M.; Zeng, H.; Murray, C. B.; O'Brien, S. P. *J. Am. Chem. Soc.* **2004**, *126*, 14583. (e) Hyeon, T.; Chung, Y.; Park, J.; Lee, S. S.; Kim, Y.-W.; Park, B. H. *J. Phys. Chem. B* **2002**, *106*, 6831. (f) Sun, S.; Zeng, H.; Robinson, D. B.; Raoux, S.; Rice, P. M.; Wang, S. X.; Li, G. *J. Am. Chem. Soc.* **2004**, *126*, 273. (g) Kang, E.; Park, J.; Hwang, Y.; Kang, M.; Park, J.-G.; Hyeon, T. *J. Phys. Chem. B* **2004**, *108*, 13932. (h) Zeng, H.; Rice, P. M.; Wang, S. X.; Sun, S. *J. Am. Chem. Soc.* **2004**, *126*, 11458. Synthesis of metal oxide nanocrystals: (i) Niederberger, M.; Bartl, M. H.; Stucky, G. D. *J. Am. Chem. Soc.* **2002**, *124*, 13642. (j) Joo, J.; Yu, T.; Kim, Y. W.; Park, H. M.; Wu, F.; Zhang, J. Z.; Hyeon, T. *J. Am. Chem. Soc.* **2003**, *125*, 6553. (k) Yin, M.; O'Brien, S. *J. Am. Chem. Soc.* **2003**, *125*, 10180. (l) Seo, W. S.; Jo, H. H.; Lee, K.; Park, J. T. *Adv. Mater.* **2003**, *15*, 795. (m) Tang, J.; Fabbri, J.; Robinson, R. D.; Zhu, Y.; Herman, I. P.; Steigerwald, M. L.; Brus, L. E. *Chem. Mater.* **2004**, *16*, 1336. (n) Seo, W. S.; Jo, H. H.; Lee, K.; Kim, B.; Oh, S. J.; Park, J. T. *Angew. Chem., Int. Ed.* **2004**, *43*, 1115. (o) Yin, M.; Gu, Y.; Kuskovsky, I. L.; Andelman, T.; Zhu, Y.; Neumark, G. F.; O'Brien, S. *J. Am. Chem. Soc.* **2004**, *126*, 6206. (p) Liu, Q.; Lu, W.; Ma, A.; Tang, J.; Lin, J.; Fang, J. *J. Am. Chem. Soc.* **2005**, *127*, 5276. (q) Yin, M.; Wu, C.-K.; Lou, Y.; Burda, C.; Koberstein, J. T.; Zhu, Y.; O'Brien, S. *J. Am. Chem. Soc.* **2005**, *127*, 9506. (r) An, K.; Lee, N.; Park, J.; Kim, S. C.; Hwang, Y.; Park, J.-G.; Kim, J.-Y.; Park, J.-H.; Han, M. J.; Yu, J.; Hyeon, T. *J. Am. Chem. Soc.* **2006**, *128*, 9753. Synthesis of rare-earth oxide nanocrystals: (s) Cao, Y. C. *J. Am. Chem. Soc.* **2004**, *126*, 7456. (t) Si, R.; Zhang, Y.-W.; You, L.-P.; Yan, C.-H. *Angew. Chem., Int. Ed.* **2005**, *44*, 3256. (u) Yu, T.; Joo, J.; Park, Y. I.; Hyeon, T. *Angew. Chem., Int. Ed.* **2005**, *44*, 7411.

(17) Park, J.; An, K.; Hwang, Y.; Park, J.-G.; Noh, H.-J.; Kim, J.-Y.; Park, J.-H.; Hwang, N.-M.; Hyeon, T. *Nat. Mater.* **2004**, *3*, 891.

in this method cannot be satisfactorily explained by the theory used to explain the "hot injection" process, in which high initial supersaturation is necessary for the formation of uniform nanocrystals.

In this Article, we present a mechanistic study on the synthesis of monodisperse iron oxide nanocrystals via "heating-up" of iron−oleate complex solution.[17] We investigated the thermal decomposition reaction of the precursor compound and fitted it to an autocatalytic process. The nucleation and growth process of iron oxide nanocrystals was traced by sampling aliquots from the reaction solution. The crystallization yield and the evolution of the size distribution of the nanocrystals were measured by analyzing these sampled aliquots. We also built a theoretical model to describe the "heating-up" process and performed a numerical simulation based on this model. Through this study, we extended the theory of the "hot injection" process to explain the formation of monodisperse nanocrystals via the "heating-up" method within the same theoretical framework.

Experimental Section

Synthesis of Iron Oxide Nanocrystals. The synthetic scheme is the same as the one reported previously.[17] Iron−oleate complex was synthesized by the reaction of iron(III) chloride ($FeCl_3 \cdot 6H_2O$, Aldrich, 98%) and sodium oleate (TCI, 95%). In a typical synthesis of iron oxide nanocrystals, 7.0 g of 1-octadecene (ODE, Aldrich, 90%) or 1-eicosene (ECE, TCI, 85%) was degassed under vacuum at 120 °C for 1.5 h, to which 1.26 g of iron−oleate complex (1.40 mmol of Fe) was added at room temperature. The resulting mixture solution was heated at a rate of 3.3 °C/min to 320 °C and held at this temperature for a given time. No additional surfactant was used.

In the following kinetic studies using thermogravimetric-mass spectrometric (TG-MS) analysis and in-situ magnetic studies, the same reaction mixture solution was used and the heating procedure was programmed in the same way as that used for the synthesis of the iron oxide nanocrystals. To trace the progress of the reaction, aliquots of the solution were sampled using a syringe. The total mass of the aliquots drawn from the solution did not exceed 15% of the total mass of the solution.

Thermogravimetric-Mass Spectrometric Analysis. An STA-MS-Skimmer Coupling (Netzsch) instrument was used for TG-MS analysis. The argon flow rate was 70 mL/min. In the mass analysis, the mass scan range was from 1 to 150 *m*/*z*.

In-Situ Magnetic Property Measurements Using Superconducting Quantum Interference Device. In-situ superconducting quantum interference device magnetometer (in-situ SQUID) measurements were carried out at 5000 Oe using a Quantum Design MPMS-7 magnetometer. The solution for the synthesis of the iron oxide nanocrystals was transferred into a quartz tube with an inner diameter of 2 mm and sealed under argon atmosphere. Because of the risk of seal breakage due to the high vapor pressure, 1-eicosene (bp 330 °C) was used as a solvent instead of 1-octadecene (bp 317 °C). After TG-MS analysis and in-situ SQUID measurement, the samples were recovered and analyzed using a transmission electron microscope.

Size Exclusion Chromatography. The sample aliquots drawn from the solution during the reaction were analyzed by size exclusion chromatography (SEC) using a Waters high-performance liquid chromatography (HPLC) system equipped with an optical absorbance detector (model 2487) and a Waters Styragel HR3 column.[18] The samples were prepared by dispersing 0.1 mL of each aliquot in 5 mL of tetrahydrofuran (THF, J. T. Baker, HPLC grade). A 0.01 M solution of hexadecylamine (HDA, Acros, 90%) in THF was used as the mobile phase, and the flow rate was 1 mL/min.

Electrochemical Impedance Spectroscopy. Samples were prepared by dispersing 0.2 mL of each aliquot drawn from the solution during the reaction in 1.0 mL of THF. AC impedance measurements were carried out by applying an AC voltage to an electrochemical cell containing the dispersion of the sample aliquots and measuring the current flowing between the working and auxiliary electrodes at room temperature. A Pt electrode of 3.0 mm diameter (Bioanalytical Systems Inc.) was used as the working electrode, and Pt wire was used as the counter electrode. The experiments were carried out in a glass cell designed to suit a two-electrode system. The impedance data were obtained using an electrochemical analyzer (CHI 660B, CH instruments Inc.) in the frequency range from 1 Hz to 100 kHz with a signal amplitude of 5 mV.

Measurement of the Crystallization Yield. The crystallization yield was calculated from the amount of iron that separated in the form of iron oxide nanocrystals from the sample aliquots drawn from the solution during the heating procedure. The iron content was measured by inductively coupled plasma (ICP) analysis. The crystallization yield was defined as $[Fe]_{crystal}/[Fe]_o$ where $[Fe]_{crystal}$ and $[Fe]_o$ are the concentration of Fe separated in the form of nanocrystals and the initial concentration of Fe, respectively.

Transmission Electron Microscopy. A JEM-2010 transmission electron microscope (Jeol) was used for the transmission electron microscopy (TEM) analysis. The size distributions of the ensembles of nanocrystals in the samples were estimated by measuring the sizes of 150−1000 particles.

Results and Discussion

Thermal Decomposition of Iron−Oleate Complex. The synthesis of the iron oxide nanocrystals was carried out by heating the solution of iron−oleate complex in a long-chain hydrocarbon solvent, that is, 1-octadecene (ODE) or 1-eicosene (ECE). When pure metal carboxylates are heated, they decompose at temperatures near to or higher than 300 °C.[19] The decomposition reaction of transition metal carboxylates occurs via the formation of thermal free radicals. The breakage of M−O and MO−C bonds of metal carboxylate results in radical species as shown in eqs 1 and 2.[19f,i]

$$M{-}OOCR \rightarrow M^{\bullet} + RCOO^{\bullet} \quad (1)$$

$$M{-}OOCR \rightarrow MO^{\bullet} + RC^{\bullet}O \quad (2)$$

These radical species can recombine, decompose into smaller molecules, or react with other metal carboxylate molecules to propagate the decomposition reaction. Usually, the thermal decomposition of metal carboxylates in the solid state leads to the formation of metal oxide along with other byproducts such as CO, CO_2, H_2, water, ketones, esters, and hydrocarbons with various chain lengths. Although some reaction equations have been suggested for the thermal decomposition of metal carboxylates, the reaction route for the formation of iron oxide and the exact stoichiometric relations are not clear.[19a,b,h,i] As

(18) (a) Wilcoxon, J. P.; Martin, J. E.; Provencio, P. *Langmuir* **2000**, *16*, 9912. (b) Farrell, D.; Majetich, S. A.; Wilcoxon, J. P. *J. Phys. Chem. B* **2003**, *107*, 11022. (c) Wilcoxon, J. P.; Provencio, P. P. *J. Am. Chem. Soc.* **2004**, *126*, 6402.

(19) (a) Davis, R.; Schultz, H. P. *J. Org. Chem.* **1962**, *27*, 854. (b) Dollimore, D.; Tonge, K. H. *J. Inorg. Nucl. Chem.* **1967**, *29*, 621. (c) Muraishi, K.; Takano, T.; Nagase, K.; Tanaka, N. *J. Inorg. Nucl. Chem.* **1981**, *43*, 2293. (d) Rozenberg, A. S.; Aleksandrova, E. L. *Russ. Chem. Bull. Int. Ed.* **1996**, *45*, 64. (e) Rozenberg, A. S.; Chukanov, N. V. *Russ. Chem. Bull. Int. Ed.* **1996**, *45*, 335. (f) Rozenberg, A. S.; Stepanov, V. R. *Russ. Chem. Bull. Int. Ed.* **1996**, *45*, 1336. (g) Langbein, H.; Christen, S.; Bonsdorf, G. *Thermochim. Acta* **1999**, *327*, 173. (h) Jesus, J. C. D.; González, I.; Quevedo, A.; Puerta, T. *J. Mol. Catal. A: Chem.* **2005**, *228*, 283. (i) Kenfack, F.; Langbein, H. *Thermochim. Acta* **2005**, *426*, 61. (j) Bronstein, L. M.; Huang, X.; Retrum, J.; Schmucker, A.; Pink, M.; Stein, B. D.; Dragnea, B. *Chem. Mater.* **2007**, *19*, 3624.

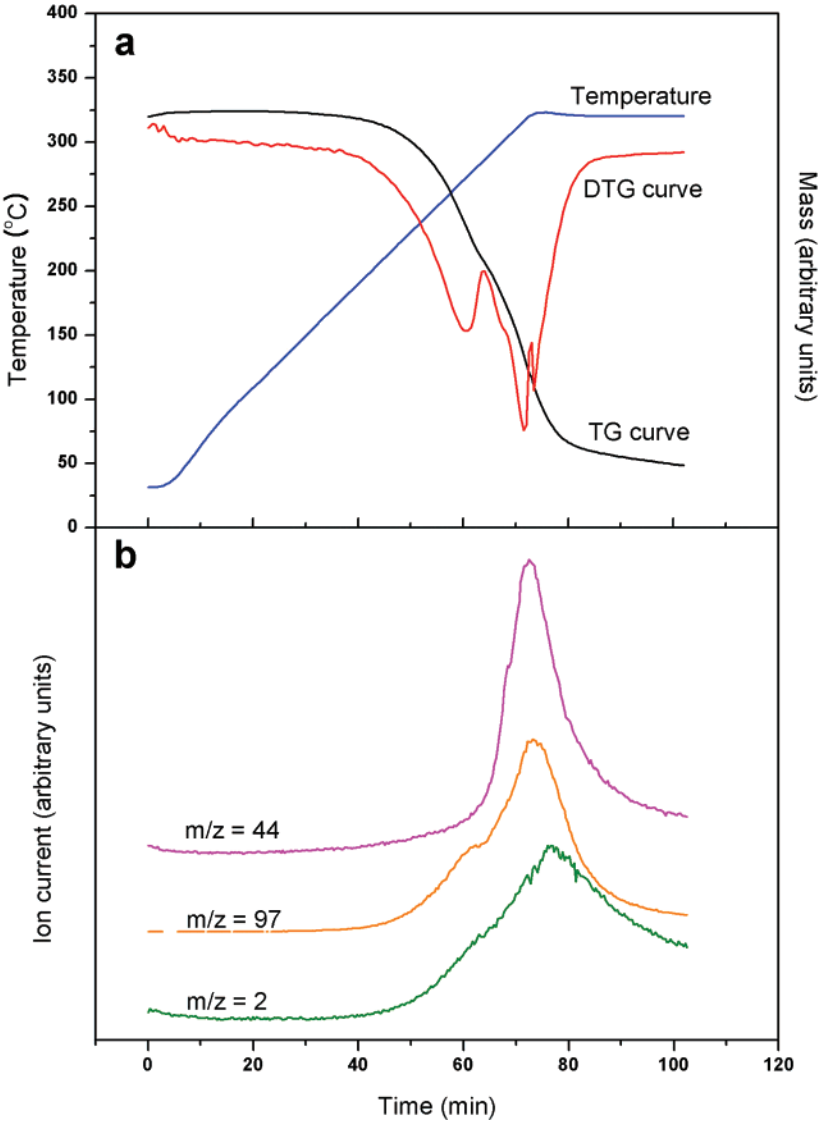

Figure 1. Thermal analysis data of the iron−oleate solution (a) and mass analysis data of the gas evolved from the solution during the thermal analysis (b) measured by TG-MS experiment. The ion current of each *m*/*z* value is proportional to the evolution rate of the corresponding compound. ECE was used as the solvent of the iron−oleate solution.

reported previously, the iron oxide nanocrystals are composed of magnetite (Fe_3O_4) and maghemite (γ-Fe_2O_3), and the composition can be written in the form $(Fe_3O_4)_x(Fe_2O_3)_{1-x}$ where x ranges from 0.5 to 0.7 depending on their size.[17] The existence of Fe_3O_4 phase means that some Fe^{3+} ions are reduced to Fe^{2+}. A recent report on the structural and compositional analysis of iron−oleate complex showed that only Fe^{3+} exist in iron−oleate complex prepared from iron(III) chloride ($FeCl_3 \cdot 6H_2O$).[19j] Consequently, it seems that a trace amount of CO, H_2, and carbon produced by the thermal decomposition of iron−oleate complex is responsible for the reduction of Fe^{3+} to Fe^{2+}.

To study the thermal decomposition process of iron−oleate complex in solution, we carried out a thermogravimetric-mass spectrometric (TG-MS) analysis. The thermogravimetric profile of iron−oleate complex in solution (Figure 1a) is very similar to that in its pure form.[17] The differential thermogravimetric (DTG) peak at 272 °C (60.5 min) is assigned to oleic acid that is either free or weakly bound to Fe^{3+} ions (see Supporting Information). The second DTG peak at 316 °C (71.5 min) matches very well with the CO_2 peak ($m/z = 44$) at 320 °C (72.5 min) in Figure 1b. Because CO_2 is one of the major products of the thermal decomposition of metal carboxylates, the peak at around 320 °C (72.5 min) can be assigned to the thermal decomposition of iron−oleate complex. Another decomposition product H_2 ($m/z = 2$) exhibited a peak at 320 °C (76.3 min). Many other hydrocarbon fragments from the thermal decomposition with *m*/*z* values in the range of 40−150 also showed broad peaks at around 320 °C (73 min). As a representative example of these fragments, the curve for $m/z = 97$ is shown in Figure 1b. No signals that could be attributed to the evolution of water or CO were detected.

To obtain more detailed information on the thermal decomposition process and the formation of iron oxide nanocrystals in the solution, the change of the magnetic moment of the reaction solution during the heating process was measured. According to previous studies on iron oxide clusters, the magnetic properties of iron-containing molecules are very sensitive to their structure and the chemical environment of Fe atoms.[20] The negative value of the baseline of the plot seems to be due to the diamagnetism of the organic molecules in the

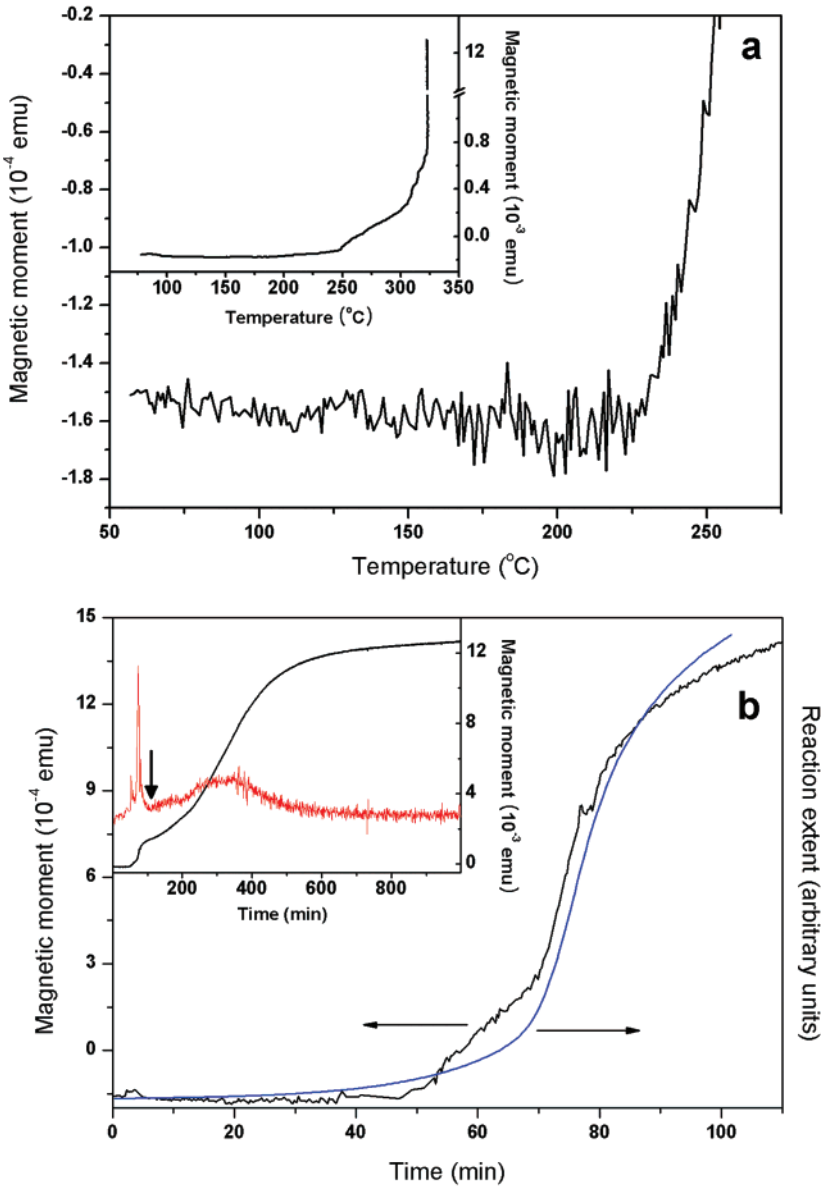

Figure 2. (a) The change of the magnetic moment of the iron−oleate solution versus temperature. The same plot in full scale is shown in the inset. (b) The same measurement data as shown in (a) replotted against time (black) and the curve for the integral of ion current intensity at $m/z = 44$ in Figure 1b (blue). In the inset, the magnetic moment curve (black) and its derivative (red) are shown (up to 1000 min). The arrow in the inset indicates the inflection point of the magnetic moment curve. The heating procedure was the same as that of TG-MS measurement up to 100 min and then it was held at 320 °C until 1000 min. The iron content in the sample solution was 4.83×10^{-4} g.

solution and the quartz tube. As shown in Figure 2a, from room temperature to about 230 °C, a slight decrease in the magnetic moment of the solution was observed, which can be attributed to the increase in the diamagnetism of quartz[21] along with the paramagnetic behavior of Fe^{3+} ions of iron-oleate complex. Following this, the magnetic moment started to increase sharply and continued to increase throughout the remainder of the heating process (the inset of Figure 2a). As shown in the inset of Figure 2b, it can be seen that the magnetic moment increased in two steps. These two steps are separated by the inflection point of the magnetic moment curve at 30 min aging at 320 °C (107 min). To examine how the increase in the magnetic moment in the first step is correlated with the kinetics of the thermal decomposition reaction, we plotted the curve for the integral of the CO_2 evolution rate in Figure 1b, which approximately represents the reaction extent of the thermal decomposition process, along with the magnetic moment curve (Figure 2b). The general trends of the two patterns matched very well. These results led us to make the following conclusions. First, the abrupt increase of the magnetic moment (Figure 2a) indicates that some structural change occurred in the iron-containing species. Second, the onset of this increase coincides with that of the evolution of CO_2 in Figure 1b, demonstrating that this structural change is correlated with the thermal

(20) (a) Gatteschi, D.; Sessoli, R. In *Magnetism: Molecules to Materials III*; Miller, J. S., Drillon, M., Eds.; Wiley-VCH: New York, 2002; pp 63−108. (b) Gatteschi, D.; Caneschi, A.; Pardi, L.; Sessoli, R. *Science* **1994**, *265*, 1054. (c) Holt, E. M.; Holt, S. L.; Tucker, W. F.; Asplund, R. O.; Watson, K. J. *J. Am. Chem. Soc.* **1974**, *96*, 2621. (d) McCusker, J. K.; Christmas, C. A.; Hagen, P. M.; Chadha, R. K.; Harvey, D. F.; Hendrickson, D. N. *J. Am. Chem. Soc.* **1991**, *113*, 6114. (e) Shiroishi, H.; Oda, T.; Hamada, I.; Fujima, N. *Eur. Phys. J. D* **2003**, *24*, 85. (f) Shiroishi, H.; Oda, T.; Hamada, I.; Fujima, N. *Polyhedron* **2005**, *24*, 2472.
(21) Marshall, B. J.; Johnson, R.; Follstaedt, D.; Randorff, J. *Rev. Sci. Instrum.* **1969**, *40*, 375.

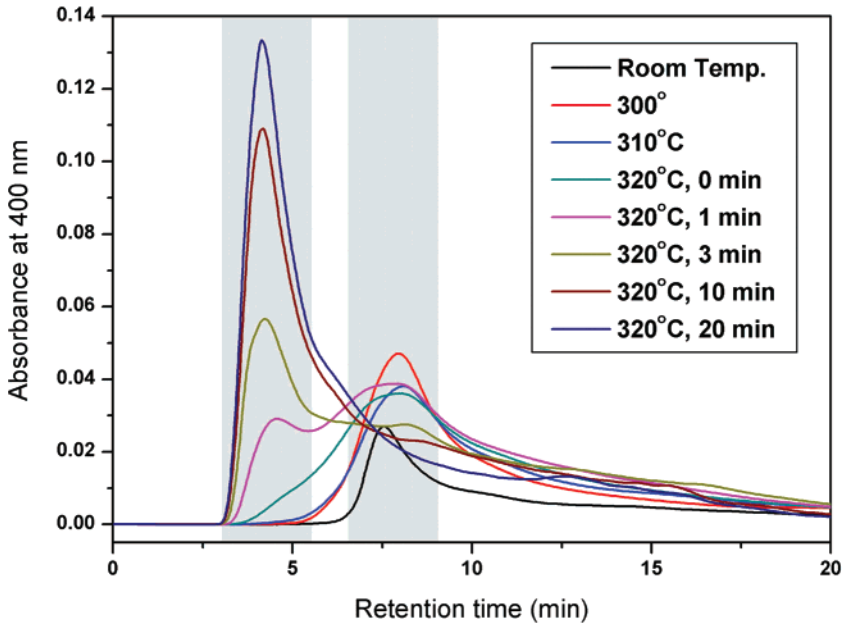

Figure 3. Chromatogram of absorbance at 400 nm of the sample aliquots drawn from the solution during the reaction for the synthesis of iron oxide nanocrystals. 1-Octadecene was used as a solvent for the reaction solution. Shaded areas indicate Region I (right) and Region II (left), respectively.

decomposition of iron−oleate complex. Third, the resemblance of the magnetic moment curve and the reaction extent curve strongly suggests that the first increase of the magnetic moment is due to the increase in the concentration of the thermal decomposition product.[22] Furthermore, we did not find any iron oxide nanocrystal in the sample aliquots taken at temperatures below 310 °C (experimental data are presented in the next section), although the thermal decomposition proceeded to a considerable extent. These results suggest that there exist intermediate species between iron−oleate complex and the iron oxide nanocrystals. Furthermore, the concentration of these species increases as the reaction proceeds until they are converted into iron oxide nanocrystals at temperatures above 310 °C in the heating procedure. It can be speculated that the intermediate species might be polyiron oxo clusters.[20b] We presume that these intermediates, rather than iron−oleate complex itself, act as monomers, the minimum building units, of iron oxide nanocrystals.

The second increase of the magnetic moment started at 30 min aging at 320 °C (107 min, the inset of Figure 2b) seems to be correlated with iron oxide nanocrystals formed in the solution because the thermal decomposition reaction has almost terminated at this time.[17] After the onset of the second increase, the magnetic moment significantly increased and then finally leveled off to 26.1 emu per gram of Fe. The mean size of iron oxide nanocrystals at the end of the in-situ magnetic measurement observed by TEM was 10.4 nm (see Supporting Information). There is little size-dependent magnetization change for superparamagnetic particles of this size range (see Supporting Information for the plots of magnetization versus size for various iron oxide nanocrystals). Consequently, this dramatic second increase of the magnetic moment seems to be mainly attributed to the increase of shape anisotropy due to the shape change of iron oxide nanocrystals from spheres to cubes under aging (see Figure 5).

Nucleation and Growth of Iron Oxide Nanocrystals. To investigate the nucleation process of the nanocrystals in the solution, we carried out size exclusion chromatography (SEC) analysis on the series of aliquots drawn from the solution during the reaction, and the results are shown in Figure 3. Because the optical absorption spectra of iron−oleate complex and iron oxide nanocrystals are almost identical in ultraviolet (UV) and visible range (see Supporting Information), we chose the absorbance at $\lambda = 400$ nm to detect both of them and the intermediate species. As shown in Figure 3, there are two ranges of retention time in which the major peaks appear, Region I from 6.5 to 9 min and Region II from 3 to 5.5 min. For the aliquots drawn from the reaction mixture below 310 °C, only one peak appeared in Region I of the chromatograms. We analyzed the same samples as those used for SEC analysis by TEM and XRD and found no iron oxide nanocrystal. Consequently, the peaks in the Region I can be attributed to iron−oleate complex and the intermediate species. In the chromatogram for the sample aliquot drawn from the solution at 0 min aging at 320 °C, a shoulder appeared in Region II indicating that some species, whose size is much larger than those of iron−oleate complex and the intermediate species, appeared in the solution. Consistent with this result, iron oxide nanocrystals were observed in the TEM analysis of the aliquot. From these results, we concluded that the nucleation process seems to start in between 310 and 320 °C. The new peak in Region II grew sharply from 1 to 20 min aging at 320 °C. Meanwhile, the peak in Region I decreased gradually and eventually vanished. During this period, the size of the iron oxide nanocrystals increased rapidly (see Supporting Information for the TEM and XRD data on the sample aliquots taken for the SEC analysis). This means that the conversion of the intermediate species into the iron oxide nanocrystals proceeded rapidly after the nucleation process started. The positions of the peaks in Region II did not change much despite

(22) The magnetic moment did not increase linearly with the concentration of the intermediate species during the heating procedure because of its temperature dependence.

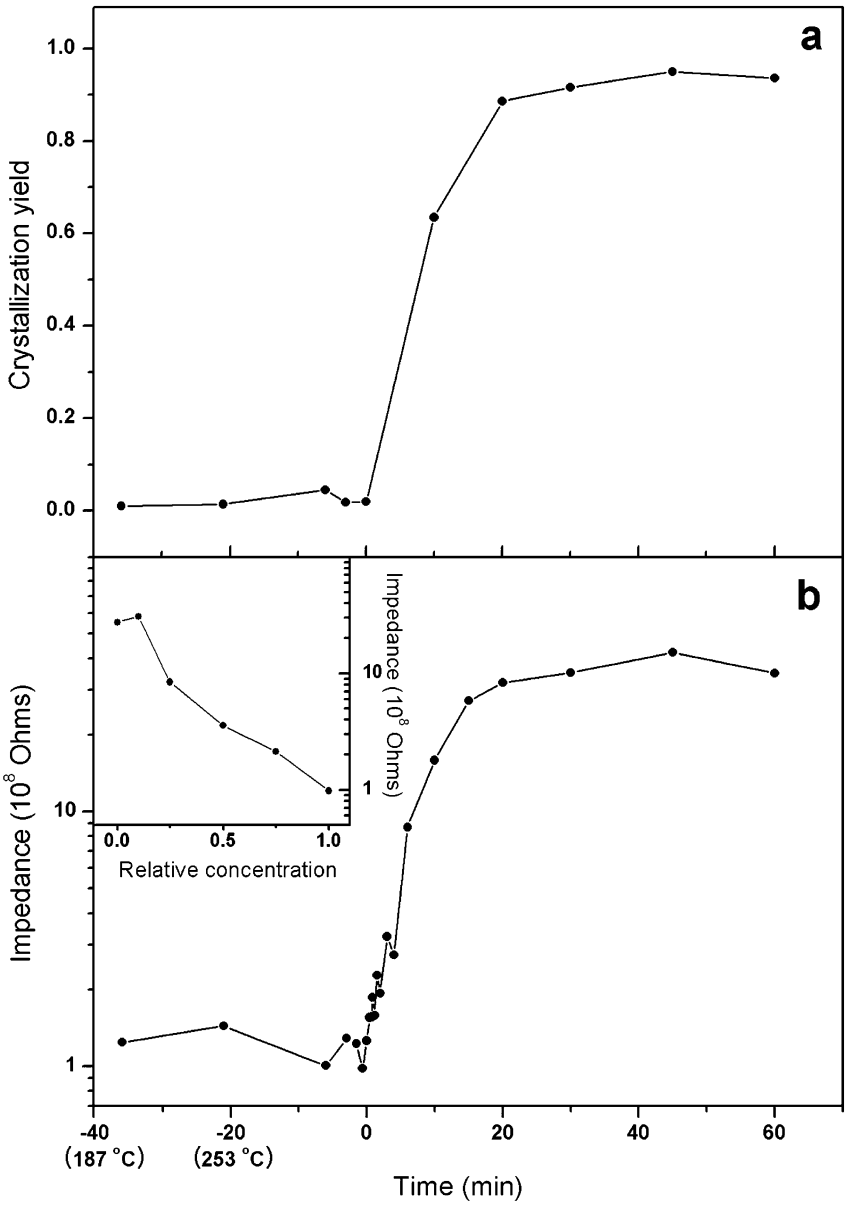

Figure 4. (a) The temporal change of the crystallization yield in the solution during the heating procedure measured by the elemental analysis. (b) AC impedance plot of the sample aliquots dispersed in THF, which were drawn from the solution during the heating procedure. In the inset, the dependence of AC impedance value on the iron−oleate concentration in the sample aliquot is plotted. Relative concentration is the iron−oleate concentration in the sample aliquot normalized by that of the original reaction solution. In the time axis in (a) and (b), $t = 0$ when the solution temperature just reached 320 °C. For $t < 0$, the corresponding solution temperature for each time is indicated in the parentheses. 1-Octadecene was used as solvent for all iron−oleate solutions.

the growth of the nanocrystals. This is because the hydrodynamic diameters of the iron oxide nanocrystals exceeded the size exclusion limit of the column.

The conversion process of the monomer to iron oxide nanocrystals was traced by measuring the time evolution of their crystallization yield. The crystallization yield was measured by two different methods, which are complementary to each other. In the first method, we separated the iron oxide nanocrystals from the aliquots and measured the iron content by the elemental analysis (ICP). The result is shown in Figure 4a. The major problem in this method is the reliability of the separation technique of the nanocrystals from the aliquots, especially in the early growth stage. To circumvent this separation problem, we adopted an alternative method using electrochemical impedance spectroscopy.[23] In our experiment, the ionic species, which can contribute to the electric conduction, are Fe^{3+}/Fe^{2+} cations and oleate anion. As the nucleation and growth process proceeds, Fe^{3+}/Fe^{2+} cations are converted into iron oxide nanocrystals, and the oleate anions adsorb on the nanocrystals or thermally decompose. These changes increase the impedance of the sample dispersion because the mobility of the nanocrystal is much lower than that of any ionic species in the solution. Consequently, we expected that the crystallization yield could be estimated by measuring the impedance of the aliquots. However, to apply this method to measure the crystallization yield, we had to make the assumption that the conductivity of the intermediate species is not very different from that of iron−oleate complex in the

(23) (a) Chang, S.-C.; Yang, Y.; Wudl, F.; He, G.; Li, Y. *J. Phys. Chem. B* **2001**, *105*, 11419. (b) Roto, R.; Villemure, G. *J. Electroanal. Chem.* **2002**, *527*, 123. (c) Kataoka, H.; Saito, Y. *J. Phys. Chem. B* **2002**, *106*, 13064. (d) Yoo, J.-S.; Song, I.; Lee, J.-H.; Park, S.-M. *Anal. Chem.* **2003**, *75*, 3294. (e) Murugan, A. V.; Reddy, M. V.; Campet, G.; Vijayamohanan, K. *J. Electroanal. Chem.* **2007**, *603*, 287.

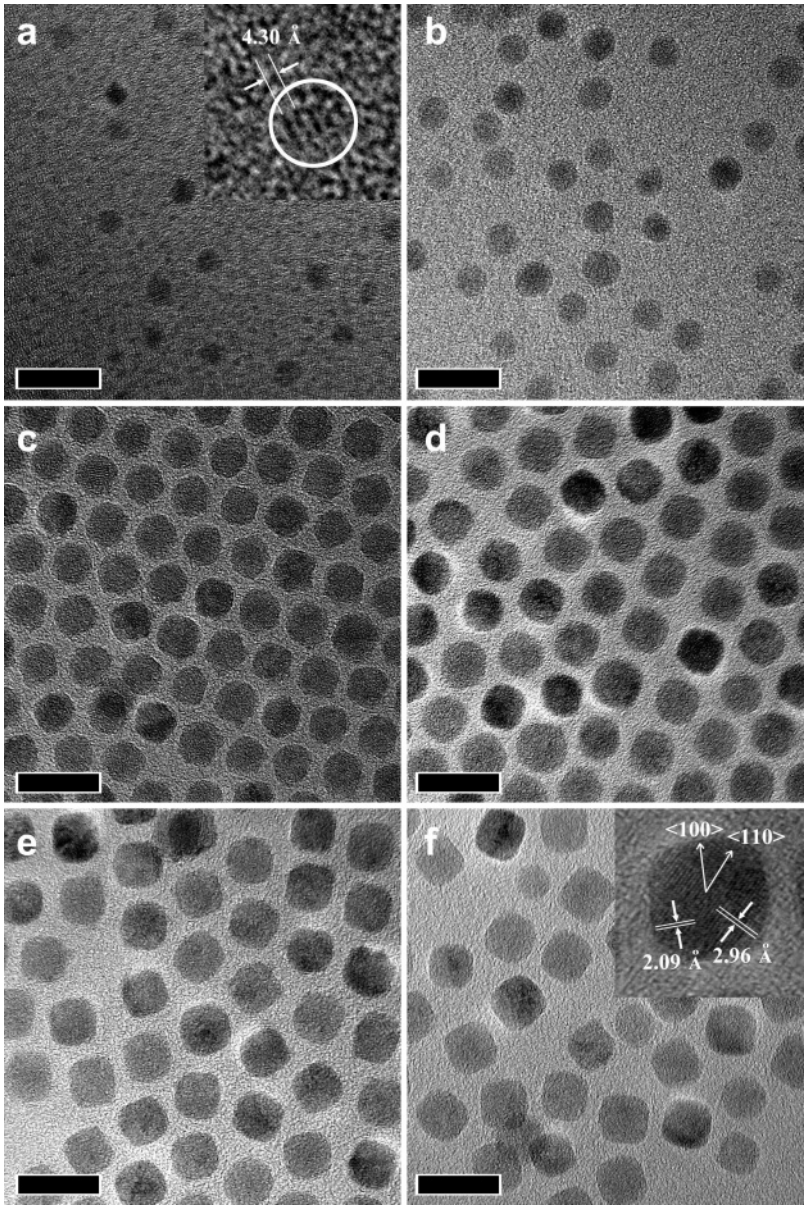

Figure 5. TEM images of iron oxide nanocrystals in the sample aliquots drawn from the solution at 320 °C being aged for 0 min (a), 1 min (b), 3 min (c), 6 min (d), 20 min (e), and 1 h (f). In the inset of (f), the *d*-spacing values observed, 2.09 and 2.96 Å, correspond to (400) and (220) planes in spinel structure of iron oxide crystal, and the zone axis was [001]. All scale bars are 15 nm.

dispersion. This assumption can be justified as long as the intermediates are molecular species containing few Fe and oleate ions, as discussed in the previous section.[20a−d] The impedance values of the dispersions of the aliquots drawn from the reaction solution are plotted in Figure 4b (see Supporting Information for the Bode plots of iron−oleate dispersions in THF and the recovery data). Referring to the calibration plot in the inset, it can be seen that the change in the log of the impedance value from 10^8 to 10^{10} Ω is directly proportional to the crystallization yield.[24] The plots of the crystallization yields measured using these two independent methods are nearly identical. In these two plots, the crystallization yield remained near zero until the solution temperature reached 320 °C, demonstrating that nearly no iron oxide nanocrystal was formed. Following this, the crystallization yield increased rapidly until 20 min aging at 320 °C, and then became saturated. These results are consistent with the SEC data shown in Figure 3.

To trace the growth process of iron oxide nanocrystals, we obtained TEM images of the series of the aliquots drawn from the reaction solution during the heating procedure. The TEM image of the aliquot taken at 317.5 °C, which was 45 s before it reached 320 °C, showed particles with mean diameter of 1.40 nm. These small nanocrystals were observed until 1.5 min aging at 320 °C. In Figure 5a, it can be seen that these small nanocrystals coexisted with larger ones during this period. Considering the time during which they existed and their nearly fixed size, the small nanocrystals seem to be at the stage just after they nucleated in the homogeneous solution. If this is the case, from the size distribution data, it can be deduced that the nucleation process terminated no later than 2 min aging at 320 °C. The high-resolution TEM (HRTEM) image of a nanocrystal whose size is about 1.72 nm is shown in the inset

(24) The AC impedance values for the samples were obtained by averaging impedance values at frequencies between 100 and 1000 Hz.

of Figure 5a as a representative one for the small nanocrystals. The *d*-spacing observed was 4.30 Å. The *d*-spacings of bulk iron oxide crystal closest to this value are 4.82 and 4.84 Å for (111) plane in maghemite and magnetite, respectively. The lattice contraction resulting from the high surface free energy and the shape anisotropy might be responsible for the discrepancy between these values.[2h,i,6] From Figure 5a−c, it is shown that the nanocrystals grew quickly and that their size became uniform after 3 min aging at 320 °C. In the following 3 min aging, their surface became smoother and rounder, while their growth rate slowed down, as can be seen by comparing Figure 5c and d. After that, further aging of the nanocrystals resulted in a broadening of the size distribution and the change of the particle shape from spheres to cubes (Figure 5e and f). The HRTEM image of a cube-shaped nanocrystal, shown in the inset of Figure 5f, revealed that the faces are {100} planes. In spinel structures, {100} plane is known to have the lowest surface free energy, and a cube-shaped crystal surrounded by {100} plane is known to be thermodynamically the most stable shape.[25] From the crystallization yield data shown in Figure 4, it can be seen that the change in the morphology of the nanocrystals occurred as the monomer concentration decreased. This can be explained by the ripening process of the crystal particles in the solution.[11c,26] If the monomers can dissolve from and reprecipitate on the crystal surface reversibly in the solution, they have a tendency to migrate from a higher to lower free energy region. When the monomer concentration is low, this tendency leads to the ripening process in which the intra- and inter-particle redistribution of the monomers occurs. Through this process, the morphology of the nanocrystals changes to a thermodynamically stable one with a smooth surface. Because smaller particles have higher surface free energy due to the Gibbs−Thomson effect, the monomers moved from smaller to larger particles. Thus, in addition to the morphology change, the broadening of the size distribution also occurs by the ripening process. The inter-particle redistribution of the monomers is well known as Ostwald ripening.

From the TEM data, we extracted the statistics for the size distribution of the nanocrystals and its time evolution data (Figure 6a−c). In Figure 6b, the relative standard deviation reached a maximum value of 63.9% at 15 s aging at 320 °C, and then decreased to 7.2% at 2 min aging at 320 °C. During this time, the mean size increased rapidly from 2.36 to 6.73 nm (Figure 6c). The standard deviation reached a minimum value of 5.8% at 4 min aging at 320 °C, then increased slightly, and nearly flattened out afterward. During this period, the increase in the mean size also nearly stopped. From these results, it is evident that there was a strong correlation between the change of the relative standard deviation and the growth rate of the nanocrystals during the period of the rapid narrowing of the size distribution. The detailed information for this size distribution narrowing process is shown in the form of histograms in Figure 6a. After the start of aging at 320 °C, the initial peak at <2 nm decreased, and a new peak appeared at ∼6 nm after 1 min aging at 320 °C. Through the further aging at 320 °C for longer time, the size distribution turned from bimodal to unimodal, and the width of the peak gets much narrower. From these data, it can be deduced that the termination of the nucleation process also played an important role in the size distribution narrowing process, which was further examined by estimating the number concentration of the nanocrystals.[27] As shown in Figure 6d, the number concentration increased to a maximum of 4.2×10^{-5} M at 45 s aging at 320 °C, rapidly fell to 7.4×10^{-6} M at 2 min aging at 320 °C, and flattened out afterward. It can be seen from this that the fast decrease of both the relative standard deviation and the number concentration occurred simultaneously. This provides good evidence for the correlation between the termination of the nucleation process and the narrowing of the size distribution. Moreover, the nucleation process of the nanocrystals seemed to occur at an extremely high rate during a very short time interval of <2 min. After aging at 320 °C for 20 min, the monomers in the solution were almost exhausted (see Figure 4), and Ostwald ripening occurred afterward, as discussed above. This resulted in the slow increase of the mean diameter, the broadening of the size distribution, and the decrease of the number concentration of the nanocrystals, as shown in Figure 6b−d.

In summary, the nucleation and growth process of the iron oxide nanocrystals characterized in this section is very similar to that observed in the "hot injection" process in that there is a sudden increase in the number concentration of the nanocrystals and rapid narrowing of the size distribution accompanied by a the high growth rate. This result strongly suggests that the size distribution control mechanism for "heating-up" process can be understood within the same theoretical framework as that for "hot injection" process.

A Theoretical Model for the "Heating-Up" Process and Its Simulation. In the previous sections, we showed that the synthetic process of iron oxide nanocrystals is composed of two sequential steps. The first step is the thermal decomposition of iron−oleate complex, and the second is the nucleation and growth of the iron oxide nanocrystals. Between these two steps, the intermediate species, which were generated from the thermal decomposition of iron−oleate complex, are responsible for the initial increase of the magnetic moment in Figure 2b. We assume that these intermediate species act as the monomers for iron oxide nanocrystals. This is the starting point of our discussions in this section, and we attempted to show that the size distribution control mechanism for the "heating-up" process is essentially the same as that for the "hot injection" process by three steps of argument. In the first step, we build a nanocrystal formation model by adding a monomer supply step to the nucleation and growth process of the "hot injection" model.[5b] In our model, how the monomers are supplied to the reaction system is not specified, thus making it generally applicable. In the second step, we performed a theoretical fitting for the reaction kinetics of the thermal decomposition of iron−oleate complex in the solution, which is the route for the monomer supply. In the third step, we carried out a numerical simulation using a completed model where the kinetics of the monomer

(25) (a) Davies, M. J.; Parker, S. C.; Watson, G. W. *J. Mater. Chem.* **1994**, *4*, 813. (b) Fang, C. M.; Parker, S. C.; With, G. d. *J. Am. Ceram. Soc.* **2000**, *83*, 2082. (c) Song, Q.; Zhang, Z. J. *J. Am. Chem. Soc.* **2004**, *126*, 6164.

(26) Zu, L.; Norris, D. J.; Kennedy, T. A.; Erwin, S. C.; Efros, A. L. *Nano Lett.* **2006**, *6*, 334.

(27) In calculating the mean volume of the nanocrystals, we made an approximation that the nanocrystals were sphere before 20 min aging at 320 °C and became cube afterward, based on the observations by TEM. The molar volumes of Fe in bulk maghemite and magnetite are 1.64×10^{-5} and 1.48×10^{-5} m^3 mol^{-1}, respectively. We used weighted average of those values referring to the compositions of iron oxide nanocrystals in various sizes reported previously in ref 17 and: *Angew. Chem., Int. Ed.* **2005**, *44*, 2872.

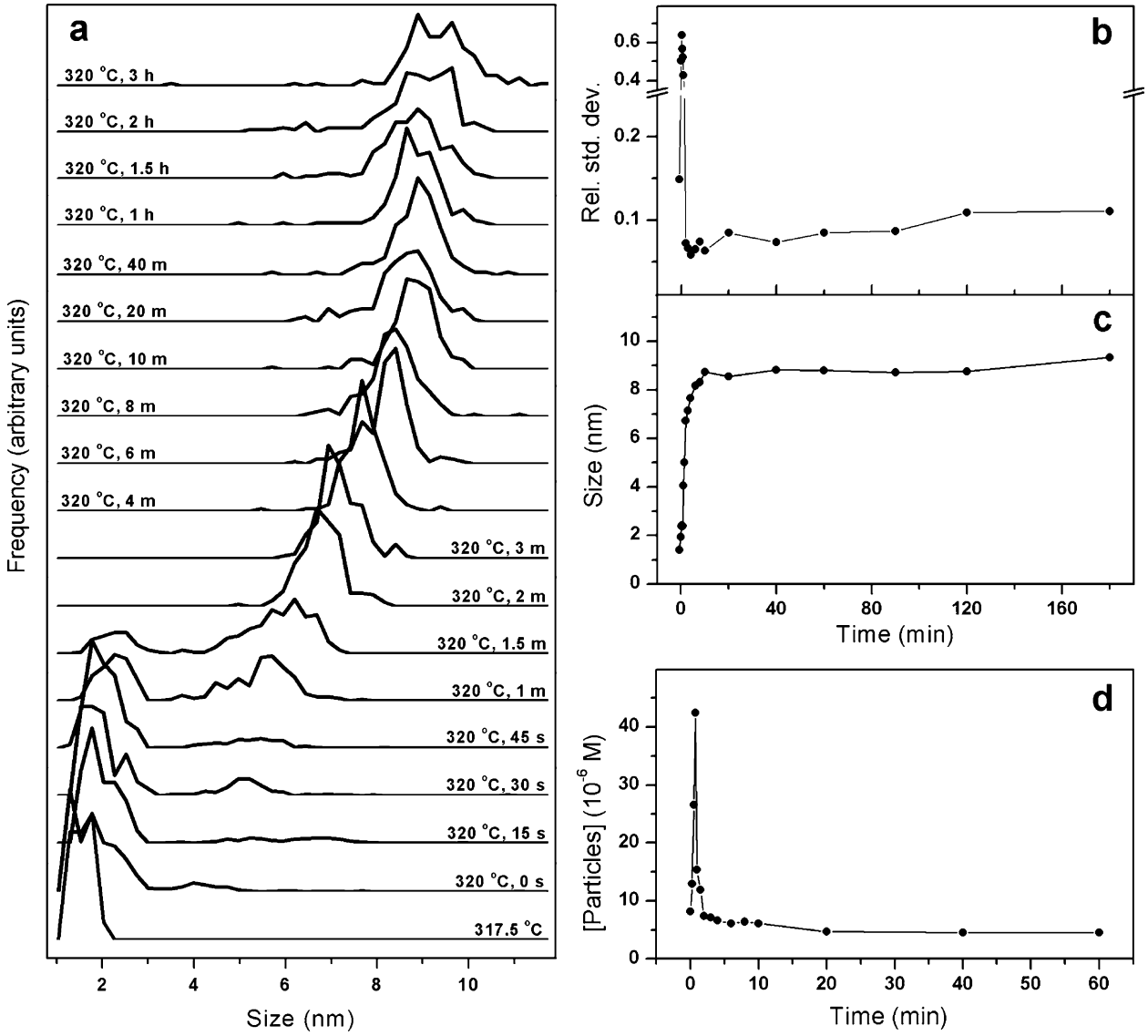

Figure 6. (a) Histograms illustrating the size distribution of iron oxide nanocrystals after aging at 320 °C for various time. For clarity, they are plotted in a line instead of a bar chart. The interval is 0.25 nm. (b,c) The time evolution of the relative standard deviation (b) and the mean size (c) of the ensemble of iron oxide nanocrystals. (d) The time evolution of the number concentration of iron oxide nanocrystals. In the time axis in (b), (c), and (d), $t = 0$ when the solution temperature just reached 320 °C.

supply obtained in the second step is incorporated into the theoretical model built in the first step.

Our theoretical model for the synthesis of the nanocrystals is composed of three processes. In the first one (Process I), the monomer, M, is produced from the precursor, P.

$$\mathrm{P} \rightarrow \mathrm{M} \tag{3}$$

Process II is the nucleation process in which crystal C is formed from the monomers:

$$x\mathrm{M} \rightarrow \mathrm{C}_x \tag{4}$$

where C_x is a crystal particle composed of x monomers. In Process III, a crystal particle can grow by acquiring more monomers in the solution via the precipitation reaction or lose monomers via the dissolution reaction.

$$\mathrm{C}_x + y\mathrm{M} \rightleftarrows \mathrm{C}_{x+y} \tag{5}$$

In this condition, the supersaturation S is defined as

$$S = [\mathrm{M}]/[\mathrm{M}]_{\mathrm{eq}} \tag{6}$$

where $[\mathrm{M}]_{\mathrm{eq}}$ is the monomer concentration in equilibrium with bulk crystal. The rate of homogeneous nucleation reaction that occurs in Process II (eq 4) is written as follows:[5b,28]

$$\frac{\mathrm{d}N}{\mathrm{d}t} = A \exp\left[-\frac{16\pi\gamma^3 {V_{\mathrm{m}}}^2}{3{k_{\mathrm{B}}}^3 T^3 {N_{\mathrm{A}}}^2 (\ln S)^2}\right] \tag{7}$$

where N is the number of crystal particles, t is time, A is a constant, γ is the surface free energy per unit area, V_{m} is the molar volume of crystal, k_{B} is Boltzmann constant, T is temperature, and N_{A} is Avogadro's number. This equation is valid only when $S > 1$. Assuming that the crystal particles are spherical, the equation for the growth rate of a particle in Process

(28) Mullin, J. W. *Crystallization*, 4th ed.; Oxford University Press: Oxford, 2001.

III is formulated in terms of the radius of the particle, r, as follows:[12d]

$$\frac{dr}{dt} = V_m D[M]_{eq}\left[\frac{S - \exp\left[\frac{2\gamma V_m}{rRT}\right]}{r + \frac{D}{k_p^\circ}\exp\left[\alpha\frac{2\gamma V_m}{rRT}\right]}\right] \quad (8)$$

where D is the diffusion coefficient of the monomer, k_p° is the precipitation reaction constant of the monomer on the surface of bulk crystal, and α is the transfer coefficient for the precipitation/dissolution reaction. This equation reflects the effect of the mass transport process of the monomers from the bulk solution to the crystal surface and the Gibbs−Thomson effect on the surface free energy of the crystal. Talapin et al. introduced a parameter, $K = (RT/2\gamma V_M)(D/k_p^\circ)$, which is very useful to indicate whether the diffusion rate or the precipitation rate of the monomer dominantly affects the growth process.[12d] For an ensemble of crystal particles, when $S \gg 1$ and/or $K \ll 1$, the smaller particles grow faster than the larger ones, leading to the "focusing" of the size distribution. On the other hand, when $S \ll 1$ and/or $K \gg 1$, the opposite effect occurs and the size distribution becomes broader.

At this stage, this model can be applied to various cases of monomer supply by incorporating appropriate reactions in Process I. In the case of the "hot injection" method, the precursors are supplied externally at the start of the synthetic process, and they either transform very quickly into the monomers or act directly as the monomers, leading to a highly supersaturated initial reaction system. In the framework of our model, this process can be described either by setting the reaction in eq 3 to proceed instantaneously or by letting P and M be identical. Actually, we already presented a simulation work in which the synthetic process of CdSe QDs by the "hot injection" method was reproduced successfully using a theoretical model similar to the one described here.[5b] On the other hand, in the synthesis of iron oxide nanocrystals by the "heating-up" method, the monomer is generated from the precursors gradually in the reaction system during the synthetic process. To model this monomer generation reaction, we investigated the reaction kinetics of the thermal decomposition of iron−oleate complex, which corresponds to Process I (eq 3) in our model.

As shown in Figure 2b, the curve for the reaction extent of the thermal decomposition of iron−oleate complex in the solution shows a sigmoidal shape, which is typical of autocatalytic reactions. It was reported that the thermal decomposition of various transition metal carboxylates and their related compounds in the solid state showed autocatalytic behavior in their reaction kinetics.[19b,d−f] Autocatalysis is a self-accelerating process in which the product reacts with the reactant to enhance the forward reaction. For the reaction in eq 3, this process is formulated in the following equation:

$$v = k[P]^\alpha[M]^\beta \quad (9)$$

where v is the reaction rate, k is the reaction constant, [P] and [M] are the concentrations of the precursor and the monomer, and α and β are the reaction orders of P and M, respectively. The reaction constant, k, is expressed in the Arrhenius form as follows:

$$k = a\exp(-b/RT) \quad (10)$$

where a and b are constants, and R is the gas constant. We fitted the reaction extent of the thermal decomposition of iron−oleate complex in the solution using eqs 9 and 10. The molar concentrations of Fe in the form of iron−oleate complex and the monomer were represented as [P] and [M], respectively.[29] The graph for the theoretical fitting was calculated by the numerical method, and the result is shown in Figure 7. As shown in this figure, the calculated reaction extent curve matches fairly well with the experimental results.

In the last step, we inserted the theoretical fitting of the thermal decomposition reaction of iron−oleate complex depicted in Figure 7 to Process I as the monomer generation reaction. With this model, we carried out a numerical simulation of the synthetic process of iron oxide nanocrystals by the "heating-up" method. In the simulation, we used the same numerical method as that which was introduced previously by our group.[5b,30] The best result is shown in Figure 8. The time evolution of the size distribution of the nanocrystals and their number concentration are reproduced quite successfully, as can be seen by comparing Figure 6b−d with Figure 8a−c and Figure 6a with Figure 8f, respectively. In Figure 8d, the time evolution of the supersaturation level is also shown, which was not observed experimentally. Comparing Figure 8c with Figure 8d, it can be seen that the monomers accumulated in the solution to a considerable extent without the nucleation of the nanocrystals. Next, the nucleation process is initiated abruptly, and the number concentration of the nanocrystals increases sharply. These results are explained by the theory of homogeneous nucleation.[11c,28] The driving force for the nucleation reaction is the difference between the chemical potential of the monomer in the solution and that in the crystal. When the solution is highly supersaturated by the monomers, they tend to form a crystal to reduce their chemical potential. However, to form a nucleus in the homogeneous solution, the driving force should be high enough to offset the increase of the free energy, which comes from the formation of the interface between the solution and the crystal. In other words, the interfacial free energy acts as an energy barrier for the nucleation reaction. Because the surface to volume ratio of a nucleus is very high, the energy barrier is high enough to prevent the nucleation reaction even at considerably high supersaturation levels. The contributions from both the driving force and the energy barrier for the nucleation reaction are reflected in eq 7. In the "heating-up" process, the solution temperature and supersaturation level increase together. As shown in eq 7, the nucleation rate is extremely sensitive to both of them. In this simulation, for example, when $T =$ 320 °C, by increasing the value of the supersaturation from 2

(29) The initial concentration of iron−oleate complex with respect to Fe was 1.58×10^{-1} mol L^{-1}, and this value was taken as $[P]_o$, the initial concentration of the precursor. The initial monomer concentration, $[M]_o$, was set to 6.0×10^{-6} mol L^{-1}, arbitrarily. The best fit was obtained with $\alpha = 2$, $\beta = 1$, $a = 16.5$ L^2 mol^{-2} s^{-1}, $b = 2 \times 10^4$ J mol^{-1}.

(30) The heating procedure and the initial precursor concentration were set identical to the synthetic process of iron oxide nanocrystals. Fe_3O_4 was regarded as a monomer, M′. The parameter values for the simulation are as follows: $V_m = 4.5 \times 10^{-5}$ m^3 mol^{-1}, $[M']_{eq} = 1.0 \times 10^{-3}$ mol L^{-1}, $\Delta t = 0.15$ s, $\gamma = 0.11$ J m^{-2}, $[P]_o = 1.58 \times 10^{-1}$ mol L^{-1}, $[M']_o = [M]_o/3 = 2.0 \times 10^{-6}$ mol L^{-1}, $A = 1.15 \times 10^{15}$ mol L^{-1} s^{-1}, $D = 1.72 \times 10^{-16}$ m^2 s^{-1}, and $K = 0.01$. The volume of the solution is 1.0×10^{-18} m^3. In the simulation procedure, the reaction rate of the thermal decomposition of the precursor, the nucleation and growth rate of the nanocrystals, and the change of the precursor and the monomer concentrations are calculated in each Δt. The crystal particles are spheres. The diameters of the nuclei just formed were drawn from the normal distribution with a mean value of 1.4 nm and the relative standard deviation of 14%. The parameters A, D, and K were adjusted to make the simulation result fit the experimental data as close as possible in terms of the size distribution and its time evolution.

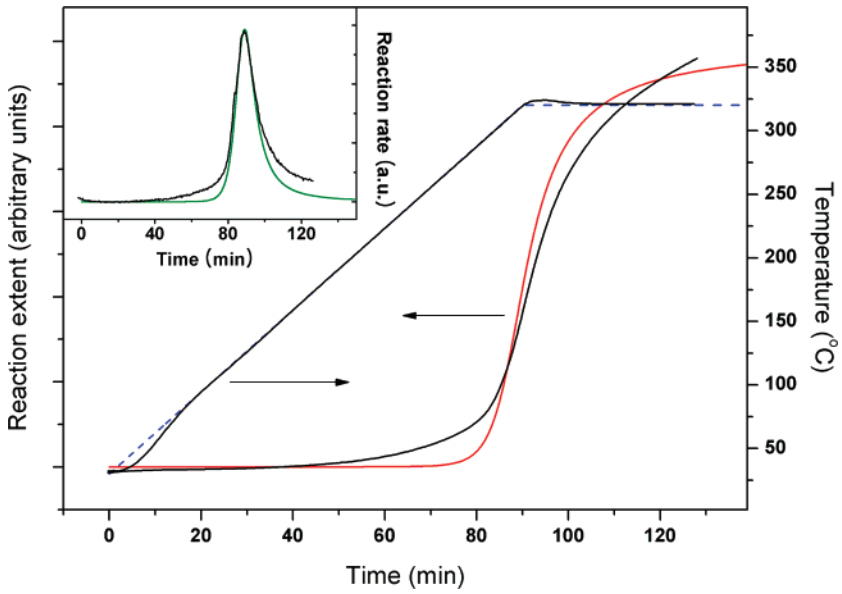

Figure 7. The plots for the reaction extent of the thermal decomposition of iron−oleate complex in the solution (black solid line), which is estimated from the evolution rate of CO_2 in Figure 1b, and its theoretical fitting (red solid line). The change of the temperature during the reaction (black dashed line) and the temperature function used for the calculation of the curve fitting (blue dashed line) are also plotted together. In the inset, the differentials of the reaction extent curve (black line) and the fitting curve (green line) are shown.

to 10, the nucleation rate is increased about 10^{190} times! As a result, the nucleation process is initiated suddenly during temperature and supersaturation is being increased as if a switch is turned on. The nucleation process persists as long as the supersaturation level is kept high enough to overcome the energy barrier for the nucleation. To keep the supersaturation level high, the monomer supply rate should be higher than or equal to the rate of the consumption of the monomer caused by the nucleation and growth of the nanocrystals. However, as the thermal decomposition reaction of the precursor proceeds, the monomer supply rate decreases and consequently the nucleation process is terminated.

In Figure 8e and f, the details of the process in which the narrowing of the nanocrystal size distribution occurred are illustrated. In Figure 8e, it is shown how the time evolutions of various factors were temporally correlated during the narrowing of the size distribution. In this figure, the formation process of the nanocrystals can be divided into three periods. The boundary between the first and second periods is the time at which the nucleation process is initiated. The second and third periods are divided by the peak position of the relative standard deviation at 308.3 °C (3.5 min before the solution temperature reached 320 °C). In the first period, only the accumulation of the monomers in the solution took place, and the nucleation process was suppressed by the energy barrier for the nucleation reaction, as discussed above. The violent fluctuation of the relative standard deviation value at the start of the second period is statistically meaningless, because there were only a few nanocrystals at that time. Next, the second and third periods are characterized by the increase and decrease of the relative standard deviation, respectively. In the second period, the most significant event is the short burst of the nucleation, which is responsible for the sharp peak of the number concentration of the nanocrystals shown in Figure 8c. In Figure 8f, it can be seen that a bimodal size distribution appear in this period, which indicates the rapid growth of the nanocrystals from the nuclei. However, due to the high nucleation rate, the proportion of the larger nanocrystals was much smaller than that of the smaller ones, and, thus, the mean diameter did not increase significantly. As a result, the combination of the rapid nucleation and growth of the nanocrystals led to the increase of the relative standard deviation in the second period. In the third period, on the other hand, the nucleation process was terminated, and only the growth process proceeded. In this period, the conditions required for the size focusing, no additional nucleation and high supersaturation, are both satisfied. As a result, the rapid growth of the nanocrystals and the fast narrowing of the size distribution took place simultaneously. In addition, the supersaturation level fell, due to the consumption of the monomer caused by the growth of the nanocrystals. The decrease of the supersaturation level resulted in a large portion of the smaller nanocrystals being dissolved away, due to their higher chemical potential, as indicated by the sharp decrease in the number concentration of the nanocrystals shown in Figure 8c. As the supersaturation level decreased, the growth rate of the nanocrystals slowed down and so did the rate of decrease of the relative standard deviation.

It is very interesting that the "heating-up" process illustrated in Figure 8e is well fitted to the well-known LaMer diagram. The LaMer model was originally devised for the monodisperse hydrosol system.[11a] Nowadays it is widely cited as a classical theory for the formation of uniform particles. The LaMer diagram shows schematically how the rapid nucleation and the separation of nucleation and growth are achieved under the condition of continuous monomer supply. In the diagram, the whole particle formation process is divided into three stages: the prenucleation stage (Stage I), the nucleation stage (Stage II), and the growth stage (Stage III) (see Supporting Information for the LaMer diagram).[11a,c] These three stages coincide with the accumulation of the monomers in the first period, the burst nucleation in the second period, and the size focusing in the third period, respectively, in the current "heating-up" process, as depicted in Figure 8e. Moreover, the simulation result of the "heating-up" process shows that the mechanism underlying the narrowing of the size distribution in this process is essentially

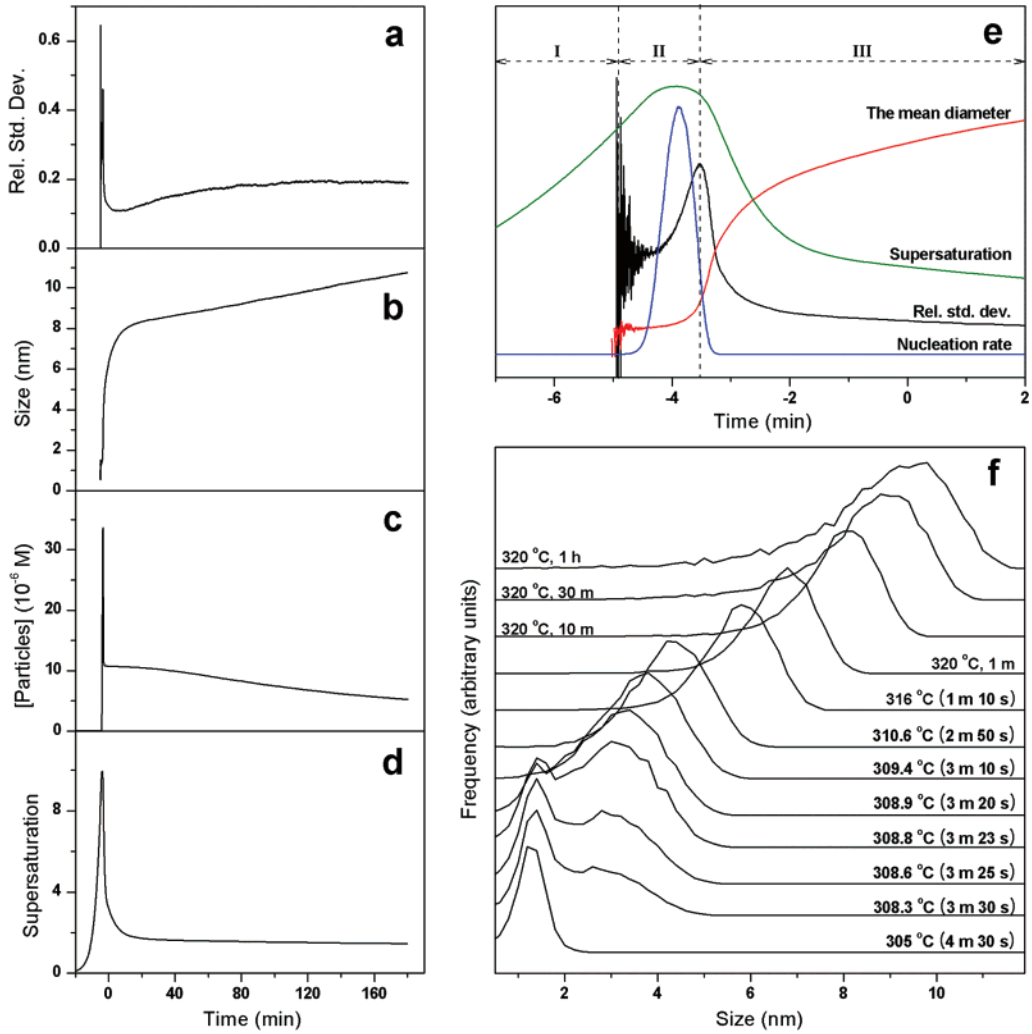

Figure 8. Simulation results of the synthetic process of iron oxide nanocrystals by "heating-up" method. (a−d) The time evolution of the relative standard deviation (a), the mean diameter (b), and the number concentration (c) of the nanocrystals and supersaturation of the solution (d). In the time axis, $t = 0$ when the solution temperature just reached 320 °C. (e) The plots shown in (a), (b), and (d) are magnified and drawn together with the time evolution of the nucleation rate. The intervals I, II, and III indicate the first, the second, and the third periods (for details, see in text). (f) Histograms illustrating the size distribution of the nanocrystals at each point of time. For the temperatures lower than 320 °C, the times remaining to reach 320 °C are indicated in the parentheses. The interval is 0.2 nm.

the same as that in the "hot injection" process. Schematically, the "hot injection" process can be regarded as a special case of the LaMer model in which Stage I is omitted.[5b,d] Consequently, the "heating-up" and "hot injection" processes share Stages II and III in the LaMer diagram.

Through the theoretical work in this section, we showed that the kinetically driven size distribution control could be achieved not only by the "hot injection" method but also by the "heating-up" method. Being different from the "hot injection" process, the generation of the monomers occurs simultaneously with the nucleation and growth of the nanocrystals in the "heating-up" process. Our simulation results imply that the burst of nucleation and the subsequent size focusing can be induced by a more diverse monomer supply mode other than "hot injection", which allows us a more versatile and flexible approach for designing synthetic schemes for monodisperse nanocrystals. In addition, we believe that our current theoretical model would be helpful to understand the size distribution control mechanism of the synthetic procedures, which were classified as the "heating-up" method in the Introduction (refs 4c, 15, and 16). In fact, there is some evidence that the synthesis of zirconia nanocrystals via the non-hydrolytic sol−gel reaction occurs in a way similar to that of the current "heating-up" process (see Supporting Information).[16j]

Conclusion

In summary, we studied the formation kinetics of iron oxide nanocrystals synthesized via the "heating-up" process by combining the experimental results with a theoretical model. The investigation of the thermal decomposition process of the precursor using TG-MS and in-situ SQUID analyses revealed the existence of intermediate species between iron−oleate complex and the iron oxide nanocrystals. We presume that these intermediates, rather than iron−oleate complex itself, act as the monomers, the minimum building units, of the iron oxide nanocrystals. The detailed studies of the nucleation and growth process using size exclusion chromatography, TEM, and the crystallization yield data showed that the mechanism underlying the formation of the nanocrystals in the heating-up process is very similar to that of the "hot injection" method, in that there is a sudden increase in the number concentration of the

nanocrystals and rapid narrowing of the size distribution accompanied by a high growth rate.

To understand the experimental results, we constructed a theoretical model describing the "heating-up" process and performed a numerical simulation. The simulation results matched well with the experimental data, and, furthermore, they are well fitted to the well-known LaMer model. Through this theoretical work, we showed that the "heating-up" process and "hot injection" method could be understood within the same theoretical framework. We expect that the concept of the "heating-up" process introduced herein can be extended to explain many other synthetic processes.

Acknowledgment. T.H. would like to thank the Korean Ministry of Science and Technology for funding through the National Creative Research Initiative Program of the Korea Science and Engineering Foundation (KOSEF).

Supporting Information Available: FT-IR spectra of the iron−oleate solution before and after the heating procedure; thermal analysis data of pure oleic acid; TEM images of iron oxide nanocrystals in the sample recovered after TG-MS analysis and in-situ SQUID measurement; FTIR and MALDI-TOF spectra of the aliquots drawn from the solution during the heating procedure; magnetization versus size plot of iron oxide nanocrystals at room temperature; optical absorption spectra of iron−oleate complex and iron oxide nanocrystals; TEM and XRD data of the sample aliquots used for SEC analysis; Bode plots of iron−oleate dispersions in THF and the recovery data; the LaMer diagram; and TG-MS and the crystallization yield data for the synthesis of zirconia nanocrystals. This material is available free of charge via the Internet at http://pubs.acs.org.

JA074633Q